A Bayesian model for inferring total solar irradiance from proxies and direct observations: application to the ACRIM Gap

T. Amdur [1*]

P. Huybers [1]

[1]Department of Earth and Planetary Sciences, Harvard University

Key Points:

- The change in total solar irradiance (TSI) across a gap in observations from 1989–1991 differs by up to 0.7 W/m^2 between reconstructions.
- A Bayesian hierarchical model is used to combine satellite and proxy observations and better constrain TSI across the ACRIM Gap.
- TSI is found to change by only 0.01 [95% CI -0.07, 0.09] W/m^2 across the ACRIM Gap, in keeping with some previous reconstructions.

*20 Oxford St, Cambridge, MA 02138, USA

Corresponding author: T. Amdur, amdur@g.harvard.edu

Abstract

Differences among total solar irradiance (TSI) estimates are most pronounced during the so-called "ACRIM Gap" of 1989–1991, when available satellite observations disagree in trend and no observations exist from satellites with on-board calibration. Different approaches to bias-correcting noisy satellite observations lead to discrepancies of up to 0.7 W/m^2 in the change in TSI during the Gap. Using a Bayesian hierarchical model for Total Solar Irradiance (BTSI), we jointly infer TSI during the ACRIM Gap from satellite observations and proxies of solar activity. In addition, BTSI yields estimates of noise and drift in satellite observations and calibration for proxy records. We find that TSI across the ACRIM Gap changes by only 0.01 W/m^2, with a 95% confidence interval of [-0.07, 0.09] W/m^2. Our results are consistent with the PMOD CPMDF and Community Consensus TSI reconstructions and inconsistent with the 0.7 W/m^2 trend reported in the ACRIM composite reconstruction. Constraints on the trend across the ACRIM Gap are primarily obtained through constraints on the drift in the Nimbus-7 satellite that are afforded by overlapping satellite and proxy observations.

Plain Language Summary

Total solar irradiance is a measure of the solar power per unit area received by Earth from the Sun. Accurately estimating total solar irradiance, and its variations, has been a longstanding methodological challenge due to the difficulty of correcting for satellite observations of total solar irradiance, especially during periods without many overlapping observers for comparison, such as during the so-called "ACRIM Gap" of 1989–1991 when no satellites with on-board calibration were observing total solar irradiance. We demonstrate the effectiveness of a Bayesian statistical model in objectively correcting satellite error during the ACRIM Gap by simultaneously taking in observations from both satellites and indirect measures of total solar irradiance such as sunspot number. This model is the first to simultaneously correct and use direct and indirect observations to reconstruct total solar irradiance. The results of the model are consistent with some past reconstructions of total solar irradiance in finding little or no change in irradiance during the ACRIM Gap, contrary to the ACRIM composite that estimated a large increase over this period.

1 Introduction

Direct measurements of total solar irradiance (TSI) from space borne instruments began in 1978. These satellite observations are necessary to determine the structure and magnitude of TSI variation in time, and have been used to produce several TSI reconstruction products (e.g. Yeo et al., 2014; Coddington et al., 2016; Dudok de Wit et al., 2017; Yeo et al., 2017; Dewitte et al., 2022). A significant source of uncertainty over the satellite TSI era, however, is the so-called ACRIM Gap, when observations from the Active Cavity Radiometer Irradiance Monitoring experiments are unavailable for 27 months between 1989–1991. During the ACRIM Gap, TSI observations are only reported by the Earth Radiation Budget Satellite (ERBS) and Nimbus-7, two satellites without on-board calibration for instrumental drift. Furthermore, Nimbus-7 shows an upward trend from 1989 to 1991, whereas ERBS shows a downward trend, and it has been unclear what corrections should be made to either satellite record (Lockwood & Fröhlich, 2008; Scafetta et al., 2019).

Following from the discrepancies in the underlying data, estimates of TSI trends from satellite observations differ according to methodological choices. The assessed change in TSI across the the ACRIM Gap is 0.71 W/m^2 in the ACRIM TSI composite (Willson, 1997; Willson & Mordvinov, 2003; Scafetta & Willson, 2019), where we define TSI change in the ACRIM Gap as the difference between mean TSI in the 365 days after the ACRIM Gap and mean TSI in the 365 days before the ACRIM Gap. The ACRIM composite es-

timates TSI during the gap by relying upon the Nimbus-7 experiment to serve as a common comparison-point for the ACRIM1 and ACRIM2 missions whose observations form the basis for the majority of the ACRIM composite.

In contrast, the change in TSI over the ACRIM Gap in the latest estimates from the Composite Physikalisch-Meteorologisches Observatorium Davos - Data Fusion (CPMDF, (Montillet et al., 2022)) and the Community Consensus TSI Composite (Dudok de Wit et al., 2017) is approximately zero. The CPMDF reconstruction pre-processes ERBS, Nimbus-7, ACRIM1, and ACRIM2 data using corrections by Fröhlich (2006), then averages several composites of TSI created using a Gaussian process regression upon the pre-processed satellite data. The Community Consensus TSI Composite uses a wavelet-based analysis to infill missing data from individual satellite records and then combines these records using an expectation-maximization approach (Dudok de Wit et al., 2017). Notably, these foregoing approaches do not permit for correcting time-evolving satellite errors that are evident from the disagreeing trends shown by satellites (Scafetta & Willson, 2019; Lockwood & Ball, 2020).

Another approach to assessing TSI change during the ACRIM Gap is to first estimate a relationship between TSI and proxies, such as sunspots and Mg-II core-to-wing ratios, then correct for satellites based upon the divergence of satellite observations from proxy models (Krivova et al., 2009; Scafetta & Willson, 2009; Gueymard, 2018; Woods et al., 2018). Such an approach to calibrating TSI proxies, however, risks missing a secular change in TSI that may not be accounted for by proxies, which are often floored during solar cycle minima (Scafetta et al., 2019). As a result, the ACRIM composite team argues that in the absence of evidence that explicitly rejects the observations of the Nimbus-7 satellite, those observations should be used as published by the original mission scientists (Scafetta & Willson, 2014).

Our approach shares similarities with the proxy correction approach, but where calibration of the proxy and satellite drift corrections are simultaneously and objectively estimated through a Bayesian hierarchical model. Such an approach was previously recommended by Dudok de Wit et al. (2017):

> One obvious, but mathematically demanding improvement [to current reconstructions], is to move from a maximum-likelihood approach to a Bayesian one (e.g., (Tingley et al., 2012)). This would provide a more natural way of merging observations that scale differently to each other, such as the Mg-II core-to-wing index or the sunspot number record.

More specifically, we combine satellite and proxy observations together in a framework that is similar to that of Tingley and Huybers (2010) but where time-evolving TSI is estimated using a Bayesian Kalman filter.

2 Data

Because our model design is predicated upon the nature of available observations, we first describe the data. For June 1984 through October 1996, a period spanning the five years before and after the ACRIM Gap, we draw from a combination of direct satellite observations of TSI and indirect magnetic activity proxies (Fig. 3 (a) and (b)). Direct TSI observations are from the five satellite observing platforms whose data are publicly available and commonly used in TSI reconstructions, namely: Nimbus-7/HF (Hoyt et al., 1992), ACRIM1/SMM (version 1) (Willson & Hudson, 1991), ERBS/ERBE (Lee et al., 1987), ACRIM2/UARS (Pap et al., 1994), and SOHO/VIRGO A+B fused TSI (version v8-2022-1-5) (Finsterle et al., 2021).

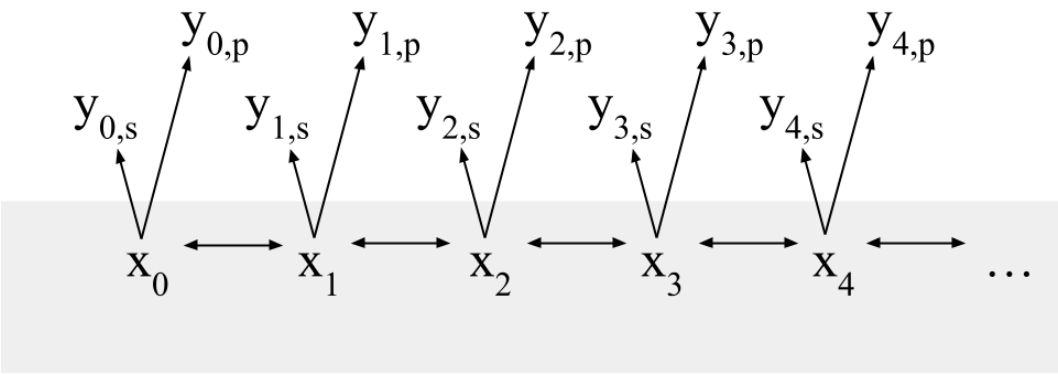

Figure 1. BTSI diagram. TSI (x_t) is represented as an auto-regressive order two process that is not directly observable (gray hidden layer). The Carter Kohn algorithm employed in BTSI uses information from across the entire time series in drawing from the conditional posterior distribution, hence the forward and backward arrows connecting the discrete times for which **x** is represented. An observation model including inferred noise and bias characteristics for each observer maps x_t into satellite observations ($y_{t,s}$) and proxy observations ($y_{t,p}$).

Two proxies for TSI are used in addition to direct satellite observations: the composite Mg-II index from the University of Bremen (version 5) (Viereck et al., 2001) and SILSO (Sunspot Index and Long-term Solar Observations) international sunspot number (version 2) (SILSO World Data Center, 1984-1996). To mitigate potential issues due to matrix operations on ill-conditioned matrices, the proxy data are normalized, scaling each variable to have a mean of zero and a standard deviation of one. Here, we report the posterior estimates of proxy parameters after rescaling back to original units.

These datasets are available at daily resolution, or bi-weekly for the ERBS/ERBE mission. Unless otherwise specified, we use the published dataset indicated as best accounting for instrumental bias and error. Observations are block-averaged to monthly resolution to facilitate computation and to focus on longer-term trends in the data, resulting in an observation array with 149 rows and 7 columns of monthly observations. To test the possibility of monthly data aliasing high-frequency TSI variability, we also ran BTSI using observations averaged over 27-day Carrington periods, but with no resulting qualitative difference in our findings relative to using monthly periods.

3 Methodology

Our Bayesian hierarchical model for Total Solar Irradiance, BTSI, infers TSI through a hierarchical, two-layer approach (Fig. 1). We first describe the layer representing the observations, which involves different representations for the proxy and direct satellite observations. The second layer represents the hidden, evolving value of TSI over time, and involves the use of a Kalman filter.

3.1 Observation Models

The first layer of BTSI relates observations to the underlying time-series of TSI. An observation from satellite s at time step t is represented as:

$$y_{t,s} = \underbrace{\begin{bmatrix} a_s & 1 & c_s \end{bmatrix}}_{\mathbf{H}_s} \underbrace{\begin{bmatrix} 1 \\ x_t \\ \tau_{t,s} \end{bmatrix}}_{\mathbf{Z}_t} + \epsilon_{t,s}. \tag{1}$$

The observation matrix ($\mathbf{H}_s$) and predictor matrix ($\mathbf{Z}_t$) combine to represent the expectation of $y_{t,s}$ as the sum of a constant offset (a_s), TSI (x_t), and a linear drift in time ($c_s\tau_{t,s}$). The time trend ($\tau_{t,s}$) is taken as the age of the satellite since its initial published observation. The values of TSI used for x_t correspond to the most recently updated estimate, which is obtained from the other layer in the hierarchy. Model TSI is initialized with the simple mean of de-meaned satellite TSI observations, and the first 500 iterations of the model are discarded to remove sensitivity to initial conditions.

The satellite offset term, a_s, is motivated by physical differences in aperture construction for TSI observing instruments over time. Since the launch of the Nimbus-7/HF instrument in 1978, estimates of the baseline solar constant have changed markedly as updated instruments have been launched, from an initial estimate of 1376 W/m^2 (Hickey et al., 1980) to a most recent estimate of 1360.8 W/m^2 (Kopp & Lean, 2011). In comparison, solar-cycle magnitude varies on the order of 1 W/m^2. The sources of offsets among satellites are well-described as a result of improvements in the apertures and cavities used for observations (Butler et al., 2008; Kopp & Lean, 2011). We report and plot TSI as an anomaly relative to the 1985–1995 mean because BTSI assesses relative offsets between satellites. Note that if these satellite offsets also reflect scaling errors in TSI variability measurements, estimating non-unitary scaling for satellite sensitivity to TSI would have only a slight effect, as (1376-1361)/1361 indicates that scaling errors are on the order of 1%.

Linear drift in satellite observations of TSI are of first-order concern. We use a linear drift term, $c_s\tau_{t,s}$, to account for the harsh conditions of the space environment that can degrade space-borne TSI instruments over time (Kopp, 2014). Effects include solar degradation of the observing cavity, aperture degradation, and changes to the thermal background (Fröhlich, 2006; Kopp & Lean, 2011). These drifts have also been empirically observed through the direct inter-comparison of overlapping satellite missions and have been shown to be dominated by a linear component (Fröhlich, 2009; Willson, 2014; Lockwood & Ball, 2020). Solar-exposure degradation can be corrected through redundant sensors, but there remain effects that can bias satellite observations. For example, two successive updates of TSI from the VIRGO (Variability of solar IRradiance and Gravity Oscillations) mission exhibited a trend difference of 0.14 W/m^2 per decade (Kopp, 2016), and linear drifts of up to 0.5 W/m^2 per decade are evident in satellite-satellite comparisons of instruments with onboard calibration (Lockwood & Ball, 2020). We report satellite drift c_s in units of W/m^2 per decade in order to provide a sense of the satellite drift that is inferred to occur over solar cycle timescales.

Normal priors are assigned to the offset magnitude, a_s, and linear time-dependent drift scaling, c_s. The prior expectation for the offset parameter a_s (μ_{a0}) is the simple average of the observations, relative to the average TSI of the ACRIM2 mission, whose instrument provides the longest record with on-board calibration in the interval examined. σ^2_{a0} is set to 5 W/m^2. We set the prior expected linear drift (μ_{c0}) to zero for each satellite, with prior uncertainty assigned a standard deviation of 0.5 W/m^2 per decade, which is larger than the empirical estimates of satellite drift found in foregoing studies (Dewitte & Nevens, 2016; Woods et al., 2018). Whereas these priors constrain the search space to allow for convergent posterior estimates, they are also chosen to permit for a wide range of plausible trends. Lastly, for the satellites, BTSI specifies that observations,

$y_{t,s}$, result from the sum of observation model predictions and Gaussian noise ($\epsilon_{t,s}$), in keeping with Dudok de Wit et al. (2017) and Montillet et al. (2022).

Similar to the satellites, an observation from proxy p at time step t is represented as,

$$y_{t,p} = \underbrace{\begin{bmatrix} a_p & b_p & 0 \end{bmatrix}}_{\mathbf{H_p}} \underbrace{\begin{bmatrix} 1 \\ x_t \\ \tau_{t,p} \end{bmatrix}}_{\mathbf{Z}_t} + \epsilon_{t,p}. \tag{2}$$

The proxy observation model differs from the satellite observation model in two respects. First, whereas we assume that satellites correctly scale the amplitude of TSI variations, the fact that proxies are not in units of TSI is accounted for by a scaling coefficient (b_p). Combined with an offset term (a_p), proxies are modeled as linearly dependent upon TSI, in keeping with a long history of this assumption (Lean et al., 1995; Lean, 2000; Fröhlich & Lean, 2004; Coddington et al., 2016). Although sunspots are directly causal of an immediate reduction of irradiance, on monthly and longer timescales they are highly correlated with increased solar activity and thus TSI (Lean, 2000; Kopp et al., 2016), such that we expect b_p to be positive on monthly timescales. When BTSI is run using only the Mg-II record, and not the sunspot record, there is no qualitative difference in results save greater overall uncertainty.

The second distinction between the satellite and proxy observation models is that no time trend is included for sunspot and Mg-II observations. We are unaware of a physical reason to assume a linear time-dependent drift in proxy observations. Although the Mg-II index is also derived from satellite data, it is calculated from a largely independent set of instruments, and its computation as a spectral ratio makes the index less sensitive to instrumental degradation effects (Thuillier et al., 2012).

Normal priors are specified for proxy coefficients a_p and b_p. The priors for amplitude scaling, b_p, are determined by regressing the proxy record upon the NRLTSI2 TSI reconstruction (Coddington et al., 2016) over the study interval. The expectation for b_p (μ_{b0}) is the estimated regression coefficient, and the prior uncertainty (σ_{b0}) is a quarter the magnitude of μ_{b0}. The prior expectation for a_p (μ_{a0}) is zero and prior uncertainty for a_p (σ_{a0}) is half the magnitude of the scaling estimate, μ_{b0}. Gaussian noise (ϵ_p) is also fit for proxy observers. In practice, proxies tend to be noisier indicators of TSI than satellites with on-board calibration, resulting in BTSI generally down-weighting proxy contributions. Importantly, however, proxies allow for a stable reference by which satellite drifts can be inferred and corrected.

3.2 Inferring Observation Model Parameters

The parameter space of BTSI is sampled using a Markov Chain Monte Carlo Gibbs sampler. For each observer n, which can be either a satellite s or proxy p, a Bayesian regression is performed using observations and a preliminary estimate of TSI to infer the observation model, $\mathbf{H}_n$, and noise parameters, ϵ_n. Specifically, under the assumption that residual errors in the model are Gaussian, posterior estimates of the model coefficient parameters, $\mathbf{H}_n$, are made through the convolution of the parameter priors and the ordinary least squares estimate for the coefficients based upon the data and predictors,

$$\underbrace{\begin{bmatrix} a_n \\ b_n \\ c_n \end{bmatrix}}_{\mathbf{H}_n} \sim \mathcal{N}\left(\begin{bmatrix} \hat{a}_n \\ \hat{b}_n \\ \hat{c}_n \end{bmatrix}, \Sigma_n \right), \tag{3}$$

where Σ_n is a covariance matrix for $\mathbf{H}_n$. The expectation and covariance matrices of $\mathbf{H}_n$ are defined as,

$$\begin{bmatrix} \hat{a}_n \\ \hat{b}_n \\ \hat{c}_n \end{bmatrix} = \left(\Sigma_{0n}^{-1} + \frac{1}{\epsilon_n^2}\mathbf{Z}_n^\intercal \mathbf{Z}_n\right)^{-1} \left(\Sigma_{0n}^{-1}\mathbf{H}_{0n} + \frac{1}{\epsilon_n^2}\mathbf{Z}_n^\intercal \mathbf{y}_n\right), \tag{4}$$

$$\Sigma_n = \left(\Sigma_{0n}^{-1} + \frac{1}{\epsilon_n^2}\mathbf{Z}_n^\intercal \mathbf{Z}_n\right)^{-1}. \tag{5}$$

Σ_{0n} is a diagonal prior covariance matrix whose entries are populated by prior uncertainties, σ_{a0}^2, σ_{b0}^2, and σ_{c0}^2. $\mathbf{H}_{0n}$ is the prior expectation for $\mathbf{H}_n$, composed of μ_{a0}, μ_{b0}, and μ_{c0} entries.

ϵ_n^2 is the estimate of observer uncertainty produced by the latest iteration of the Gibbs sampler. We follow common practice from Bayesian regression techniques and draw ϵ_n from the inverse-gamma distribution, with shape parameter, A_n, and scale parameter, θ_n,

$$\epsilon_n \sim \text{Inv-Gamma}\left(\frac{A_n}{2}, \frac{\theta_n}{2}\right). \tag{6}$$

Because the noise parameters, ϵ_n, are dependent upon a hidden TSI process and are thus difficult to constrain, stronger priors are needed than for the observation model coefficients. A_n is assigned to be $\frac{4}{3}$ times the number of observations by an observer, such that the prior estimate is assigned a third as much weight as observations in constraining the posterior estimate. For each satellite, the hyperprior (θ_{0s}) (and thus the prior expectation for ϵ_s) is established by finding the average variance of the residuals between that satellite and overlapping satellites and assigning half the observed pairwise variance to the satellite in question. Priors for ϵ_p are estimated from the average variance of the residuals of linear regression of contemporaneous satellite observations upon the proxy record.

The posterior distribution of ϵ_n, for either satellites or proxies, is drawn from the inverse-gamma distribution, such that θ_n is obtained as,

$$\theta_n = \theta_{0n} + (\mathbf{y}_n - \hat{\mathbf{y}}_n)^\intercal (\mathbf{y}_n - \hat{\mathbf{y}}_n). \tag{7}$$

$\hat{\mathbf{y}}_n$ is the observation model prediction of $\mathbf{y}_n$ and is defined as $\hat{\mathbf{y}}_n = \mathbf{H}_n^\intercal \mathbf{Z}_n$, where $\mathbf{Z}_n$ is instantiated with the latest estimate for $\mathbf{x}$. Thus, θ_n is the sum of the prior, θ_{0n}, and the squared residuals between observations and predictions (Table 1).

Table 1. Prior and posteriors for inverse-gamma parameters. Hyperparameters A_0 and θ_0 parameterize inverse-gamma distributions for the prior observer errors. A_0 are chosen such that the prior has a third as much weight as observations, and θ_0 for satellites are chosen such that the prior distribution for ϵ_{0s}^2 is centered at half the mean observed residual variance for each observer and overlapping observers.

Observer	A_0 | A	θ_0 | θ
Nimbus-7/HF	35 | 139	1.8 | 10.4
ACRIM1/SMM	21 | 82	0.6 | 1.3
ERBS/ERBE	48 | 190	3.1 | 19.0
ACRIM2/UARS	21 | 82	0.7 | 2.5
SOHO/VIRGO	3 | 12	0.1 | 0.3
Sunspot number	50 | 199	1.1E5 | 2.2E5
Mg-II index	50 | 199	4.7E-4 | 8.4E-4

3.3 State-Space Model

In the second, hidden layer of each Gibbs sampler iteration, values observed according to Eq. 1 and 2 are inverted to produce TSI estimates, $\mathbf{x}$, through a Carter-Kohn Kalman filter algorithm.

Given the complex structure of solar variability at all timescales from minutes to decades (Shapiro et al., 2017), we make the methodological choice to model TSI as an autoregressive order two process, with monthly to sub-monthly variability treated as noise. This autoregressive representation is meant to capture the autocorrelated and quasi-cyclic behavior of TSI with a minimum number of free parameters (Pankratz, 2012). We note that we find no qualitative change in results if we instead use an AR(1) or AR(3) model. The autoregressive order two representation of the time evolution of TSI anomalies is used to generate the prior expectation for TSI before concurrent observations are assimilated,

$$\hat{x}_t = \alpha_1 x'_{t-1} + \alpha_2 x'_{t-2}. \tag{8}$$

Along with a prior expectation ($\hat{x}_t$), we also generate a prior estimate of the variance of the noise in the TSI estimate (η_t). Given that month-to-month changes in TSI are closely related to the phase of solar cycle activity, we model η_t as linearly dependent upon $\overline{x}_t$, the monthly TSI anomaly relative to the 11-year running mean of TSI,

$$\hat{\eta}_t = q + m\overline{x}_t, \tag{9}$$

$$q \sim \mathcal{N}(\mu_q, \sigma_q^2), \quad m \sim \mathcal{N}(\mu_m, \sigma_m^2), \tag{10}$$

where q and m are regression parameters for the intercept and slope, respectively, of the expectation of noise variance $\hat{\eta}_t$ as a function of $\overline{x}_t$. The observations of η_t used to fit this regression are determined by finding the residuals between $\mathbf{x}$ and $\hat{\mathbf{x}}$ for the most recent estimate of $\mathbf{x}$. The careful specification of priors for η_t is important, as a hidden layer model conditioned upon only the data is unable to discern between the TSI uncertainty implied in satellite TSI records versus proxy models of TSI that miss real components of solar variability, such as the added noise from superimposing sunspot darkening with facular brightening, and are thus more smoothly varying and autocorrelated. The priors for q and m are estimated by fitting Eq. 9 to the monthly TSI innovations of the NRLTSI2 TSI reconstruction over the 1984–1996 period and using the resulting likelihood distribution as a prior distribution (Table 2).

This formulation for the hidden layer gives a time-varying estimate of TSI variability, including during sparse data intervals such as the ACRIM Gap. Because nearly half of observations in the study interval are from proxies that predict lower month-to-month variability than satellites, the posterior estimates of η_t are lower than the prior. These posterior estimates serve as caution against using BTSI for reconstruction of high frequency TSI variability: the average month-to-month autocorrelation of BTSI monthly estimates is $r = 0.95$, whereas the inferred month-to-month autocorrelations of the CPMDF and ACRIM composite TSI records are $r = 0.80$ and $r = 0.87$, respectively. While the posterior TSI uncertainty of BTSI is inaccurate, autocorrelated process models for TSI have been successfully implemented in the past and high-frequency variability can be reintroduced in such models (Montillet et al., 2022). For the purposes of estimating the change in TSI over a longer period such as the ACRIM Gap, however, reintroduction of high-frequency variability is unnecessary, as will be shown in Sec. 4.

BTSI obtains a posterior distribution of x_t, called x'_t, by updating the prior expectation, $\hat{x}_t$, with observations,

$$x'_t = \hat{x}_t + \underbrace{\sum_{s=1}^{n_s} K_s \left(y_{t,s} - \hat{y}_{t,s|\hat{x}_t}\right)}_{\text{sat.-based innovation}} + \underbrace{\sum_{p=1}^{n_p} \frac{K_p}{b_p} \left(y_{t,p} - \hat{y}_{t,p|\hat{x}_t}\right)}_{\text{proxy-based innovation}} . \tag{11}$$

Table 2. Prior and posterior estimates of state-space model parameters q and m are in units of W/m^2, while the α_1 and α_2 parameters are dimensionless. Note that while a conjugate prior distribution is not specified for α_1 or α_2, we ensure stability of the model by resampling α if $|\alpha| \geq 1$.

Parameter	Prior [95% CI]	Posterior [95% CI]
α_1	–	0.92 [0.67, 1.17]
α_2	–	0.05 [-0.19, 0.30]
q	0.0025 [0, 0.038]	0.015 [0, 0.026]
m	0.16 [0.11, 0.21]	0.07 [0.04, 0.11]

The last two groupings in Eq. 11 describe the adjustment of the prediction using observationally-derived estimates. The Kalman gains (K_s and K_p) are dimensionless values representing the relative weighting of satellite and proxy data relative to $\hat{x}_t$, where weights increase with the inferred accuracy of an observer. The inclusion of b_p in the last grouping reflects a necessary conversion of proxy units to W/m^2.

3.4 Inferring State-Space Model Parameters

For each realization of the Gibbs sampler, the first two autoregressive parameters (α_1 and α_2) are computed from the most recent estimate for the state vector, $\mathbf{x}$,

$$\underbrace{\begin{bmatrix} \alpha_1 \\ \alpha_2 \end{bmatrix}}_{\alpha} \sim \mathcal{N}\left(\begin{bmatrix} \hat{\alpha}_1 \\ \hat{\alpha}_2 \end{bmatrix}, V_\alpha \right). \tag{12}$$

The expectations $\hat{\alpha}_1$ and $\hat{\alpha}_2$ are determined from multiple linear regression of $\mathbf{x}$ upon lag-1 and lag-2 realizations of $\mathbf{x}$, and V_α is a diagonal matrix whose nonzero entries are the scaled variance of the residuals of the autoregression model. Stability of the autoregressive model is enforced by redrawing estimates of α_1 and α_2 if $|\alpha| \geq 1$.

For satellites, the Kalman gain is calculated as a function of the prior TSI variance (v_t) and observer error, ϵ_s:

$$K_s = v_t \left(v_t + \epsilon_s^2 \right)^{-1}. \tag{13}$$

For proxies, the Kalman gain must also consider the scaling of proxy units to those of TSI:

$$K_p = b_p^2 v_t \left(b_p^2 v_t + \epsilon_p^2 \right)^{-1}. \tag{14}$$

The prior for TSI variance, v_t, is a covariance matrix containing the covariance structure of x_t and x_{t-1}. v_t carries over the posterior variance estimated for the last time step, v'_{t-1}, and adds to the first diagonal entry the prior expectation of TSI variance at time step t, η_t^2:

$$v_t = \alpha^\intercal v_{t-1} \alpha + \eta_t^2. \tag{15}$$

Similar to the update for the expectation of TSI, the updated estimate of the TSI variance (v'_t) is found by updating the prior estimate of TSI variance according to the observations:

$$v'_t = v_t - v_t \left(\sum_{s=1}^{n_s} K_s + \sum_{p=1}^{n_p} K_p \right). \tag{16}$$

After one iteration of the Kalman filter is run for all time steps $t = 1, 2, ..., T$, the Carter-Kohn algorithm is used to efficiently sample from the posterior conditional distribution for x_t (Carter & Kohn, 1994). Because both observational and process noise

Table 3. Observer error structure used in synthetic TSI experiment. Observation model parameters for a_n (in units of W/m^2 for satellites) are randomly drawn from $\mathcal{N}(0, 0.5)$ and added to the mean offset from the ACRIM2 average. Scaling for b_p is estimated from regression on the NRLTSI2 reconstruction, and c_n (in units of W/m^2 per decade) is assigned by randomly permuting the linear drifts inferred by BTSI.

Observer	a_n	b_n	c_n
Nimbus-7/HF	11.0	1	0.17
ACRIM1/SMM	6.3	1	0.62
ERBS/ERBE	4.1	1	-0.41
ACRIM2/UARS	4.2	1	0.08
SOHO/VIRGO	-0.3	1	0.24
Sunspot number	-42	145	0
Mg-II index	-4.9E-3	0.013	0

is assumed to be Gaussian, the joint posterior distribution of TSI, conditional upon the data, $p(\mathbf{x} \mid \mathbf{y})$, is multivariate normal and can be factorized,

$$p(\mathbf{x} \mid \mathbf{y}) = p(x_T \mid \mathbf{y}) \prod_{t=1}^{T-1} p(x_t \mid x_{t+1}, \mathbf{y}). \tag{17}$$

Once the Kalman filter is fully run forward such that the expectation and variance estimates, x'_T and v'_T, have been estimated for the final time step T, an estimate is drawn for the last time step x_T from $p(x_T \mid \mathbf{y})$. Estimates are then sequentially drawn for $t = T-1, ..., 1$ in order to generate x_t from $p(x_t \mid x_{t+1}, \mathbf{y})$ for all time steps. The Carter-Kohn approach has been successfully implemented in many Bayesian Kalman filter models, most prominently in monetary policy modeling by Bernanke et al. (2005). See Ch. 3 of Blake et al. (2012) for a more-detailed walk through of the Carter-Kohn algorithm implementation used in BTSI.

We run a Gibbs sampler for 10,500 iterations of the two-layer model on a single chain, discarding the first 500 iterations as a burn-in period. This approach leads to adequate sampling of the 149 monthly TSI parameters and 24 model parameters contained within BTSI. We assess the capability of a 10,000 iteration run to obtain a stable posterior marginal distribution by calculating the potential scale reduction metric ($\hat{R}$). $\hat{R}$ is an estimate of the factor by which the scale of the posterior distribution would be corrected by allowing the chains to fully range over the distributions if the number of iterations is allowed to approach infinity (Gelman et al., 2013). Running three initially-dispersed chains then splitting each chain in half to generate six intervals for comparison, we calculate that the potential scale reduction metric $\hat{R}$ is between 1 and 1.015 for all parameters of interest when using a 10,000 iteration chain, suggesting that our posterior estimates are close to convergence with the exact posterior marginal distribution.

4 Evaluation of Model through Synthetic Data Experiments

We test the performance of BTSI under three scenarios for TSI history between 1984 – 1996: that CPMDF represents true TSI anomalies (referred to as CPMDF-All), that the ACRIM composite is true (ACRIM-All), and a hybrid scenario where proxies record TSI anomalies from CPMDF but satellites record TSI from the ACRIM composite (ACRIM-Satellite/CPMDF-Proxy). CPMDF-All represents a null case where essentially no secular change in TSI occurs during the ACRIM Gap, with TSI 0.02 W/m^2 larger in the year after the gap compared to the year before. ACRIM-All, in contrast, repre-

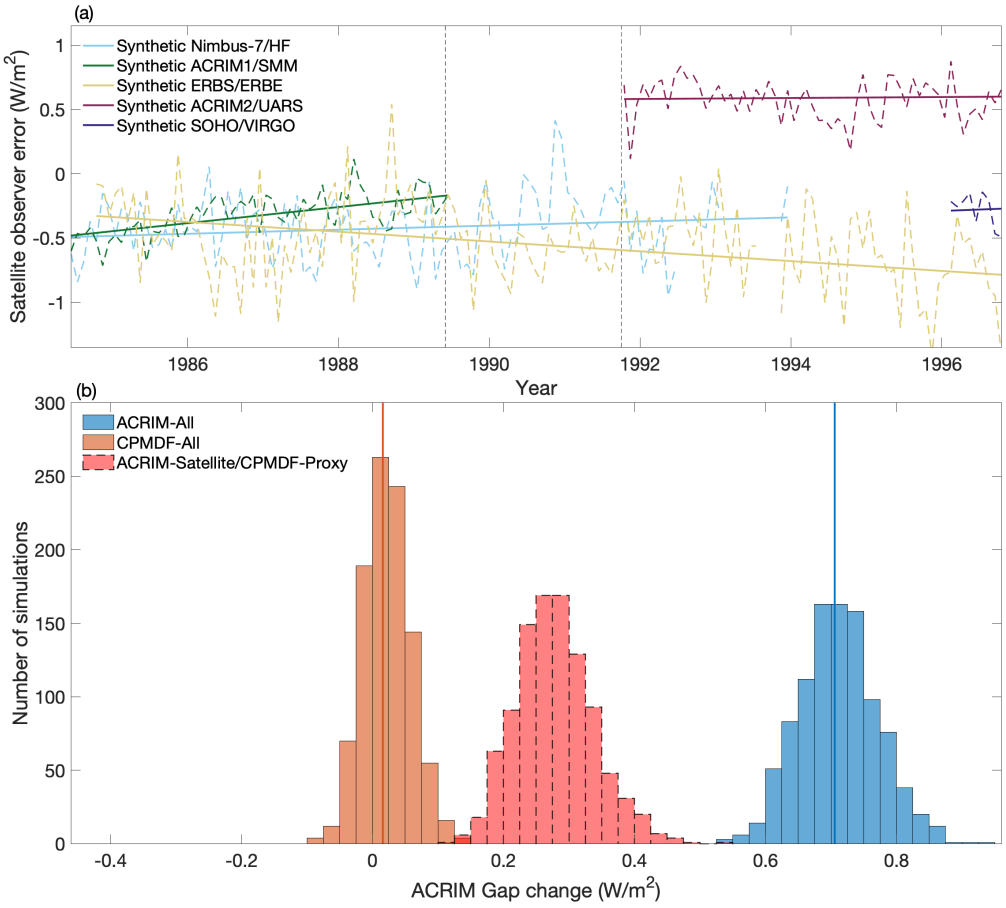

Figure 2. BTSI inferred ACRIM Gap under three TSI scenarios. (a) Observer error structure of satellites used in all three scenarios. Solid lines indicate the offsets and linear drifts imposed in all realizations of synthetic data, and dashed lines are an example of a single synthetic dataset that includes AR(1) noise. BTSI is run upon 1000 synthetic datasets for each of three scenarios and the resulting histograms of differences in TSI across the gap are shown in (**b**). The three scenarios are for the ACRIM-All (blue), CPMDF-All (orange), and ACRIM-Satellite/CPMDF-Proxy (dashed red) scenarios. The true gap magnitudes for the ACRIM-All and CPMDF-All scenarios are shown by a vertical line. BTSI estimates of the ACRIM-Satellite/CPMDF-Proxy ACRIM Gap are above the 95% level of the CPMDF-All scenario for all 1000 estimates.

sents a TSI increase of 0.71 W/m^2 in the year after the gap compared to the year before. ACRIM-Satellite/CPMDF-Proxy represents a scenario wherein proxies function as a red herring: they are sensitive to solar cycle variability, but insensitive to inter-cycle variability in the true value of TSI that only satellites are able to record.

To test each scenario, we produce synthetic datasets of observations using the observation model framework given in Eqs. 1 and 2. Thus, synthetic satellite and proxy records are produced by multiplying an observation matrix $\mathbf{H}_n$ with a predictor matrix $\mathbf{Z}_n$ instantiated with the TSI history from one of the three scenarios. To allow for simple comparison, all synthetic datasets are initialized with the same set of observation matrices, $\mathbf{H}$ (Table 3).

After realizing observation matrix parameters, we generate one thousand synthetic datasets of TSI for each scenario with the same coverage as the actual observational record, i.e. data gaps and observations occur at the same time as in the actual record. Each synthetic dataset is uniquely generated by adding random observer noise to the results from $\mathbf{H}_n^{\intercal}\mathbf{Z}_n$. Synthetic proxies are given Gaussian noise with variance equal to the noise variance, ϵ_p^2, that BTSI infers for the proxy records. Synthetic satellite records are generated by adding AR(1) noise, in keeping with the autocorrelation that has been empirically found in satellite residuals (Dudok de Wit et al., 2017). The AR(1) parameter for the satellite noise generation process is set to 0.34, the value we empirically estimate to be the AR(1) parameter of detrended residuals of overlapping satellite records from this time period. The variance of the AR(1) time series for each satellite is set to match the inferred noise variance, ϵ_s^2, BTSI infers for each satellite from real observations. The presence of AR(1) noise in the synthetic satellite record differs from the observation model assumption of BTSI, wherein observational noise in satellites is assumed independent. By adding AR(1) noise, we test the ability of BTSI to accurately infer changes to TSI even in the event of autocorrelated noise in satellite observing instruments.

For each synthetic dataset, we run BTSI and record the inferred magnitude of the change in TSI over the ACRIM Gap, as well as the 95% confidence interval of that estimate provided by the model. The distribution of ACRIM Gap magnitudes inferred from the resulting 1000 BTSI runs are plotted as histograms (Fig. 2 (b)). BTSI distinguishes between the ACRIM-All and CPMDF-All scenarios in all cases. The mean and 95% range of CPMDF-All is 0.02 [-0.04, 0.09] W/m^2, whereas it is 0.71 [0.60, 0.84] W/m^2 for ACRIM-All. Both 95% ranges encompass the true change in TSI across the ACRIM Gap for their respective scenarios and exhibit no bias. The 95% confidence intervals estimated by BTSI exhibit good coverage, with 984/1000 of 95% confidence intervals in the CPMDF-All experiment and 944/1000 of the 95% confidence intervals in the ACRIM-All experiment inclusive of the true ACRIM Gap. This is due to the confidence intervals being closely aligned with the empirically-derived 95% range, with the average 95% confidence interval estimated as 0.17 W/m^2 for CPMDF-All and 0.23 W/m^2 for ACRIM-All, compared to the empirically-derived range of 0.14 W/m^2 for the CPMDF-All experiment and 0.24 W/m^2 for ACRIM-All.

The ACRIM-Satellite/CPMDF-Proxy scenario results illustrate the mechanics of how BTSI performs in practice. Because BTSI determines satellite drift through both satellite-satellite comparison and satellite-proxy comparison, information about a secular change in TSI is still retained by the model through satellite comparison even in the event that the proxies contain no information about long-term TSI change. Thus, the estimate of the ACRIM Gap in this scenario is between the CPMDF-All and ACRIM-All scenarios (0.27 [0.18, 0.41] W/m^2), consistent with BTSI assigning roughly equal weight to both satellite and proxy sources. The ACRIM-Satellite/CPMDF-Proxy scenario estimates of the ACRIM-Gap are significantly displaced from the CPMDF-All scenario, with all 1000 BTSI estimates of the ACRIM-Satellite/CPMDF-Proxy scenario significantly different at the $p = 0.05$ level from the CPMDF-All estimates. This supports a conclusion that, even if proxies are not sensitive to a secular shift in TSI, no shift in

Table 4. Prior and posterior estimates of observation model parameters. Prior and posterior maximum likelihoods are provided along with posterior 95% confidence intervals in brackets. Priors are indicated by the subscripted 0, for example in a_{0s}. Offsets, a_{0s} and a_s, are in units of W/m^2 relative to a mean value of 1364.3 W/m^2, as estimated from ACRIM2, which is taken as a reference level. Proxy scalings, b_{0p} and b_p, are in units converting W/m^2 to the units of the observing index. Linear satellite drifts, c_{0s} and c_s, are in units of W/m^2 per decade. For proxies, each ϵ_p is scaled by b_p such that both ϵ_s and ϵ_p are in units of W/m^2.

Source	a_{0s}	a_s	b_{0s}	b_s	c_{0s}	c_s	ϵ_{0s}	ϵ_s
Nimbus-7/HF	7.8	7.5 [7.4, 7.6]	1	1	0	0.62 [0.37, 0.85]	0.2	0.27 [0.24, 0.31]
ACRIM1/SMM	3.0	3.0 [2.9, 3.1]	1	1	0	-0.41 [-0.71, -0.11]	0.23	0.13 [0.11, 0.16]
ERBS/ERBE	1.0	0.8 [0.8, 0.9]	1	1	0	0.17 [0.02, 0.33]	0.18	0.32[0.28, 0.35]
ACRIM2/UARS	0	0 (reference-level)	1	1	0	0.07 [-0.28, 0.43]	0.17	0.18 [0.15, 0.21]
SOHO/VIRGO	-3.6	-3.3 [-3.5, -3.2]	1	1	0	0.24 [-0.75, 1.22]	0.23	0.15 [0.09, 0.26]

Source	a_{0p}	a_p	b_{0p}	b_p	c_{0p}	c_p	ϵ_{0p}	ϵ_p
Sunspot number	89	66 [56, 76]	145	167 [150, 185]	0	0	0.33	0.20 [0.17, 0.23]
Mg-II index	0.16	0.16 [0.15, 0.16]	0.013	0.014[0.013, 0.016]	0	0	0.26	0.14 [0.12, 0.17]

long-term TSI of the magnitude proposed by the ACRIM composite occurred during the ACRIM Gap if BTSI estimates are consistent with zero change in TSI during the gap. The synthetic experiments lend confidence to applying BTSI to the actual set of observations.

5 Results of Application to Actual Observations

Application of BTSI to our collection of satellite and proxy observations indicates minimal changes in TSI across the ACRIM Gap and strong evidence against the increase of 0.71 W/m^2 indicated by the ACRIM composite. Specifically, TSI across the ACRIM Gap is estimated to increase slightly by 0.01 W/m^2, with a 95% confidence interval of [-0.07, 0.09] W/m^2 (Fig. 3 (c)). Specifically, the 95% confidence interval for the change in TSI during the ACRIM Gap encompasses the CPMDF and Community Consensus TSI Composite estimates and excludes the estimate from the ACRIM composite.

Differing magnitudes of standard error are inferred among observing satellites (Fig. 4 (c)). The ERBE and Nimbus-7 instruments have a median inferred standard error of 0.32 and 0.27 W/m^2, respectively, whereas the ACRIM1, ACRIM2, and SOHO satellites are inferred to have standard errors of 0.13, 0.18, and 0.15 W/m^2, respectively. Such differences in standard error are expected because, unlike later satellites, ERBS and Nimbus-7 satellites were unable to perform on-board calibration. The inferred precision of each observer directly affects their relative contribution towards estimates of TSI (Fig. 5).

Estimates of satellite drifts are also key in determining the trend across the ACRIM Gap (Fig. 4 (b)). Drift estimates are obtained through a joint intercomparison between overlapping satellite estimates as well as proxy observations. Satellites with longer observing intervals generally afford greater constraint upon associated estimates of linear drift. ERBS, with 142 months of recorded observations in our dataset, has a 95% confidence interval for posterior linear drift of 0.31 W/m^2 per decade, whereas the VIRGO instrument aboard SOHO, with only 9 months of observations in the study period, has a 95% confidence interval for posterior linear drift of 1.97 W/m^2 per decade, despite having a lower standard error.

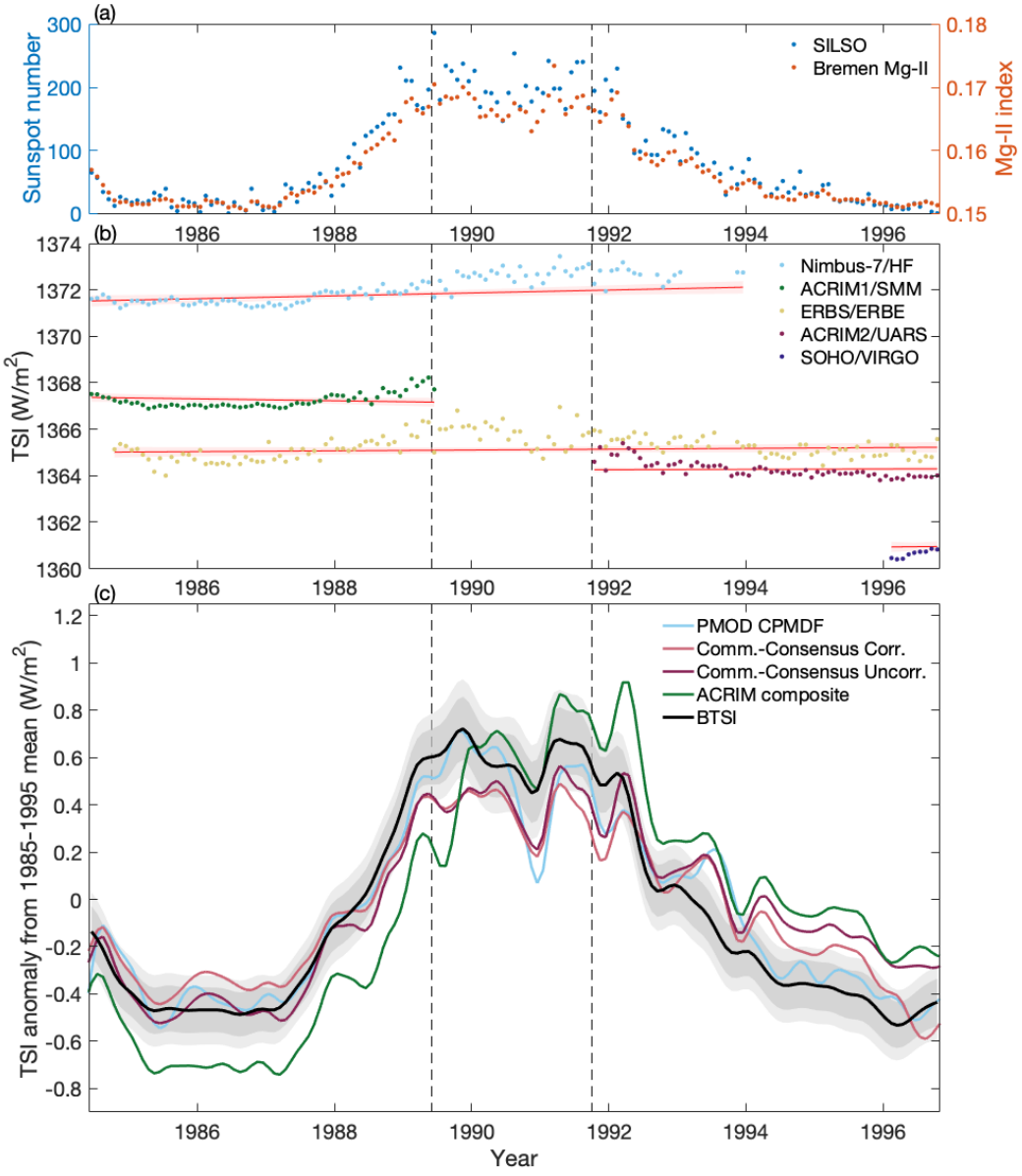

Figure 3. Data used in our analysis and comparison of TSI variability in selected reconstructions. **(a)** Monthly SILSO sunspot number (blue) and Univ. of Bremen Mg-II index values (orange) used in BTSI. **(b)** Monthly satellite TSI observations used in BTSI. Maximum likelihood estimates of offset and linear drift are shown in red with 99% confidence interval in pink. **(c)** Comparison of selected reconstructions. All TSI reconstructions are displayed as 6-month-smoothed average anomalies from the 1985-1995 mean. Reconstructions include CP-MDF (Montillet et al., 2022) (blue), two versions of the Community Consensus TSI Composite v 1.1 (Dudok de Wit et al., 2017), with Fröhlich (2006) pre-corrections (pink) and without pre-corrections (magenta), and ACRIM composite (Willson & Mordvinov, 2003) (green). The most likely estimate from BTSI is displayed in black, with 80% and 95% confidence intervals in dark and light gray, respectively. Dashed lines bracket the ACRIM Gap.

Based upon the inferred precision of the available observers, BTSI assigns roughly 60% weighting to the sunspot count and Mg-II index during the ACRIM Gap and 40% to the Nimbus-7/HF, and ERBS/ERBE records (Fig. 5). Correcting for an estimated 0.62 W/m^2 per decade drift in Nimbus-7 observations and assigning weight to ERBS/ERBE observations essentially nullifies the positive trend between the nadirs of Solar Cycles 21 and 22 found in the ACRIM composite and, to a lesser-extent, the Community-Consensus TSI Composite. Correcting for smaller drifts in ERBS and ACRIM2 TSI records leads to a slight upward adjustment in the amplitude of Solar Cycle 22 compared to the CPMDF and Community Consensus composites.

The BTSI approach is novel in its ability to determine time-dependent uncertainty in TSI, as evidenced by the confidence intervals estimated in the synthetic data experiments. From the posterior distributions of our Bayesian approach, composed of 10,000 draws of TSI estimates at each timestep, time-dependent estimates of uncertainty are produced. Fig. 3 (c) shows the resulting BTSI estimate after correction for observer artifacts, including the maximum likelihood estimate (black) and the 80% and 95% confidence interval (dark and light gray). The peak two-sigma uncertainy of 0.44 W/m^2 occurs in April 1991 due to the confluence of an active solar cycle period when solar activity is larger and the loss of high-fidelity instruments during the ACRIM Gap. The minimum two-sigma uncertainty of 0.29 W/m^2 occurs in September 1986, during a period of reduced solar activity. The 95% confidence intervals produced by BTSI encompass almost all observations from the CPMDF reconstruction, whereas ACRIM composite TSI estimates deviate significantly.

6 Discussion and Conclusion

BTSI results contrast with the ACRIM composite in that we find no evidence of a secular change in TSI during the ACRIM Gap. The ACRIM composite relies upon observations from the ACRIM satellites and infilling from the Nimbus-7 satellite during periods when observations from an ACRIM mission are unavailable, including the ACRIM Gap. The ACRIM composite relies on spliced intervals of satellite observations where satellite offsets are corrected but, critically, where no provision is made for drifts in satellite observations.

Central to our findings is the inferred drift of Nimbus-7. Drift is constrained both in in relation to proxy estimates and to the ACRIM satellites with on-board calibration. The demeaned Nimbus-7 observations are plotted against the TSI indicated by other contemporaneous observers in Fig. 6 after correcting the other observers for offsets, scaling, and drift according to results from BTSI. Due to the inferred observational noise in the uncalibrated ERBE instrument aboard ERBS, the observations of Nimbus-7 do not consistently deviate from ERBS at a statistically significant level. For the calibrated ACRIM1 and ACRIM2 satellites, however, as well as the predictions of TSI from Mg-II and international sunspot number, Nimbus-7 shows clear signs of drift before and after the ACRIM-Gap. Nimbus-7 observations of TSI are consistently below the adjusted estimates from all contemporaneous observers during 1988 – 1990, and the October 1988 – January 1989 period shows Nimbus-7 observations below the 90% range of all non-ERBS observers. In contrast, after the ACRIM Gap, every monthly observation of Nimbus-7 contemporaneous with ACRIM2 is above the ACRIM2 best estimate, with 6 out of 16 monthly observations outside the 99% confidence interval of ACRIM2 estimates.

The offsets between Nimbus-7 and other observers underlie the BTSI estimate of a drift in Nimbus-7 of 0.62 [0.37, 0.85] W/m^2 per decade. Various alternative implementations of BTSI result in similarly significant drift estimates, including running BTSI without any observations from ERBS, which results in a Nimbus-7 drift estimate and 95% confidence interval of 0.53 [0.28, 0.77] W/m^2 per decade. Our results differ from the ACRIM composite in point of incorporating Nimbus-7 observations after correcting for instru-

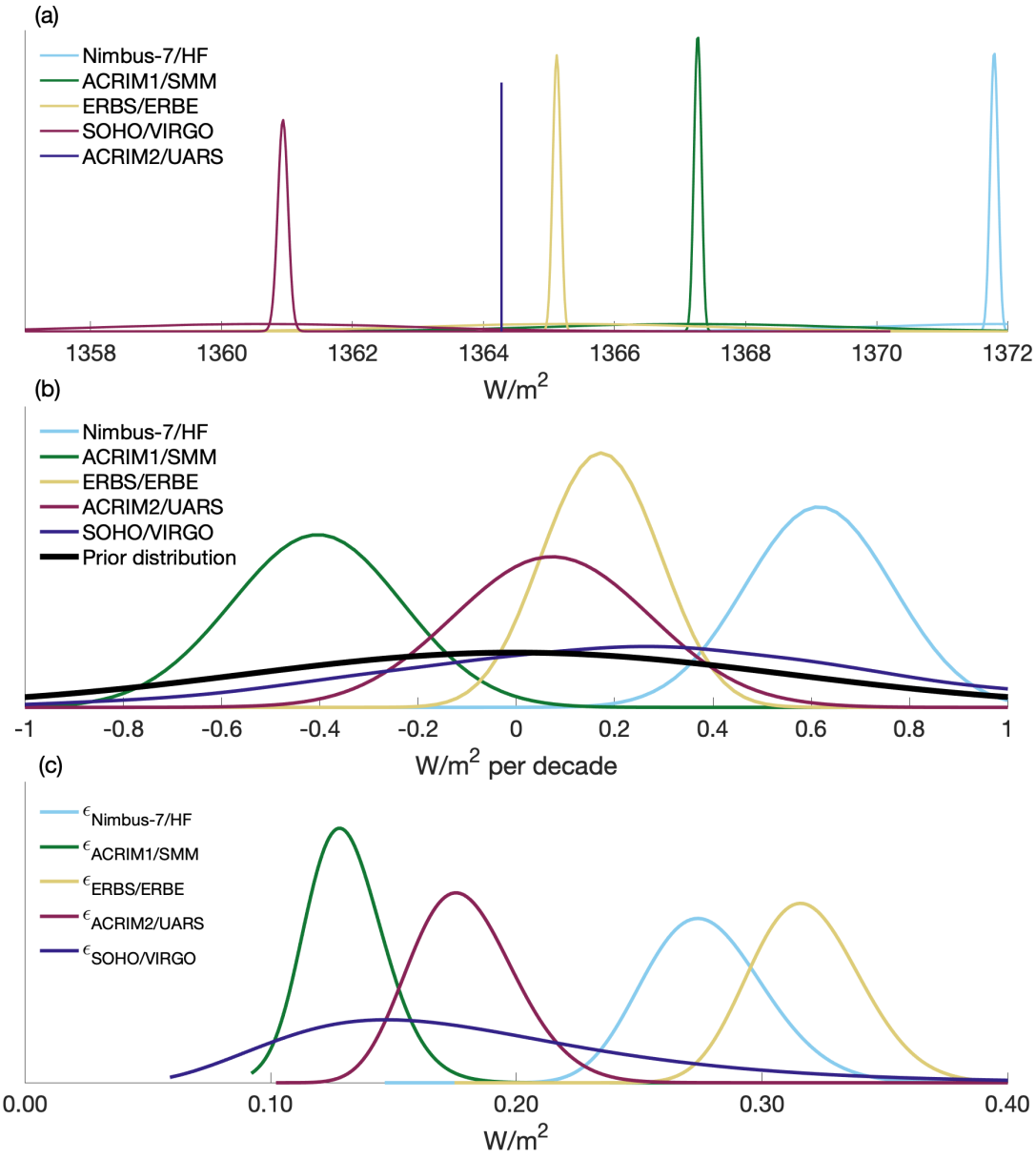

Figure 4. Priors and posteriors for satellite parameters. (a) Priors (flat curves) and posteriors (sharp curves) for offsets a_s. The ACRIM2 mean TSI value is taken as a reference level, hence its appearing as a delta function. **(b)** Priors and posteriors for time-dependent linear drifts, c_s. The normal prior distribution (black) and smoothed empirical posterior distributions are plotted. All satellites begin with the same prior expectation of 0 W/m^2 per decade and standard deviation 0.5 W/m^2 per decade. **(c)** Posterior inverse-gamma distributions for observational noise ϵ_s. Note that the hyperparameters of the inverse-gamma prior distributions are provided in Table 1 but are not shown here for readability.

mental drift. Nimbus-7 receives 11% to 16% of the weighting of BTSI predictions before the ACRIM Gap and 16% to 21% during the ACRIM Gap (Fig. 5).

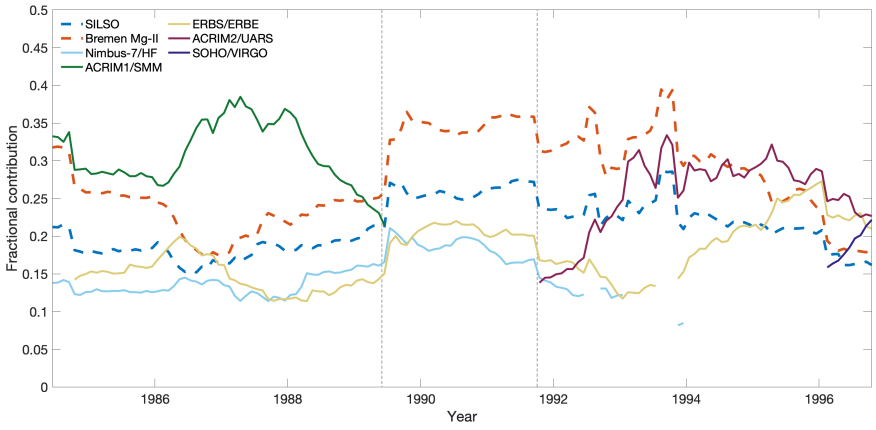

Figure 5. Contribution of each observer to the TSI estimate. Fractional contributions from proxies (bold dashed) and satellite TSI observations (solid) to the monthly innovation of the TSI process. Contributions are computed as the mean across all iterations of the Gibbs sampler and are smoothed with a 36-month filter. Dashed lines bracket the ACRIM Gap.

The findings of BTSI generally lend support to the CPMDF reconstruction. The CPMDF reconstruction is based on corrected Nimbus-7, ERBS, and ACRIM1 satellite observations, where corrections are based upon comparison to proxies and degradation curves for instruments of similar design (Fröhlich, 2006). The linear drifts inferred by BTSI for Nimbus-7 and ERBS — the two satellite records observing for the longest duration within the 1984 to 1996 period that we focus on — are consistent with those inferred by Fröhlich et al. (2006). Fröhlich et al. (2006) estimate a linear drift of 0.81 W/m^2 per decade for Nimbus-7 and 0.23 W/m^2 per decade for ERBS. The 95% confidence intervals of linear drift by BTSI for Nimbus-7 and ERBS are inclusive of both estimates. The Fröhlich corrections to ACRIM1 include a hyperbolic correction in response to a hypothesized darkening of the aperture early on during its mission. Because BTSI assumes linear corrections, it is more difficult to compare the Fröhlich ACRIM1 correction and the BTSI linear correction. Although BTSI is based on linear corrections to satellites, an examination of the residuals between the data and the model predictions reveals that a nonlinear function could potentially offer a more accurate representation of satellite errors for some observers, such as ACRIM1. However, the added complexity of a nonlinear satellite error model may be difficult to constrain and does not appear necessary for this particular analysis.

A number of other studies have examined proxies of TSI in relation to satellite observations, and they generally agree with CPMDF, the Community Consensus Composite, and BTSI results in finding no substantial change in TSI across the ACRIM Gap (Gueymard, 2018; Lee III et al., 1995; Woods et al., 2018). The utility of BTSI lies in the ability to consider information from satellite and proxy sources simultaneously. Satellites and proxies are combined in a consistent statistical framework to calibrate the proxies and identify drift and offsets in satellites. We highlight that BTSI would be expected to identify changes in TSI across the ACRIM Gap, were a substantial change to exist, even if the proxies did not register such a change, as illustrated in the synthetic ACRIM-Satellite/CPMDF-Proxy (Fig. 2) Our synthetic results also suggests BTSI would detect major nonlinear or secular changes in the relationship between proxies and TSI.

Over the full satellite era of 1978 to present, the longer observing periods of satellites, larger number of satellite instruments examined, and higher rates of satellite over-

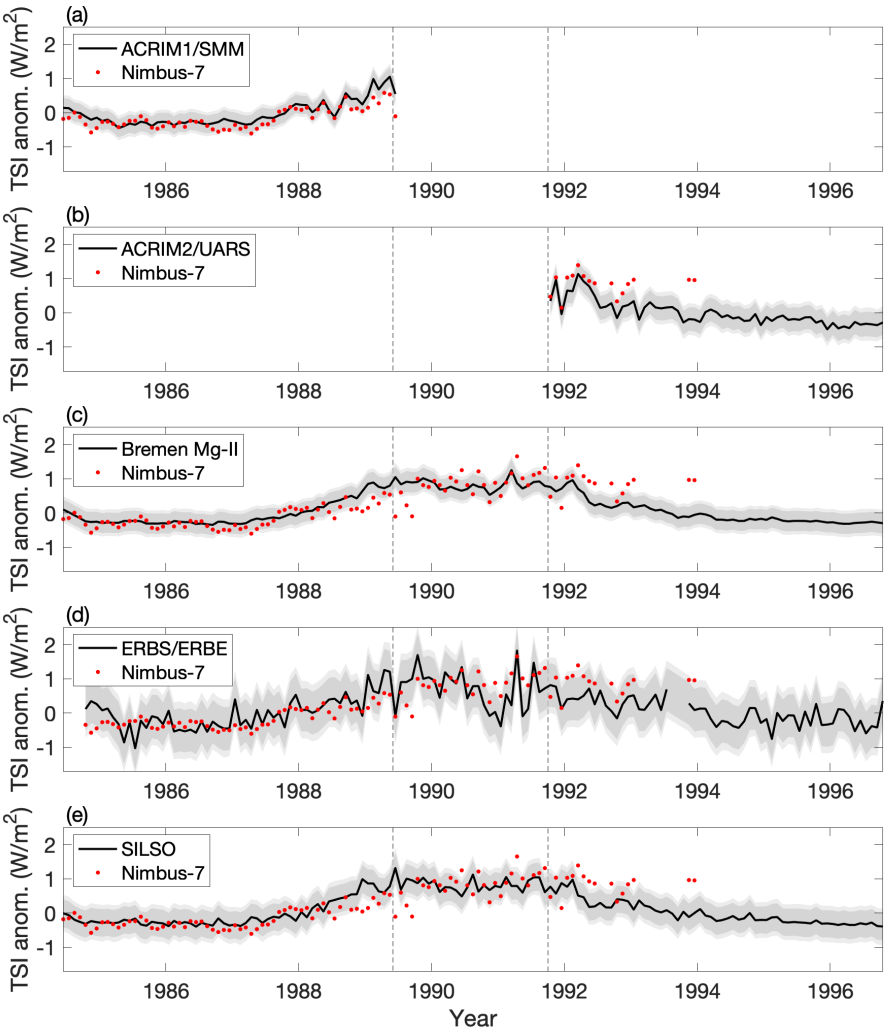

Figure 6. Comparison of Nimbus-7 observations against other TSI indicators. Nimbus-7 observations (red dotted) are compared against other contemporaneous TSI indicators. All observations are demeaned, and other TSI indicators are additionally scaled or corrected for linear drifts. The maximum likelihood estimate of TSI is shown (black lines) along with 90% (dark gray) and 99% confidence intervals (light gray). Confidence intervals are calculated by including the uncertainty in drift, offset, and observational noise as indicated by 10,000 draws of BTSI. Dashed lines bracket the ACRIM Gap period.

lap should all lead to higher-confidence posterior estimates of satellite noise and bias structure. The use of BTSI over longer intervals thus holds promise for inferring TSI variability over multidecadal periods inclusive of uncertainty estimates. The BTSI methodology may also be applicable on multi-centennial timescales, where proxies would then form the basis of TSI reconstructions.

Open Research

BTSI output over the ACRIM Gap is available as a NetCDF file from the Harvard Dataverse repository (doi:10.7910/DVN/JBDZYQ). BTSI was written in Matlab R2020b, with all code used to generate the figures and output published on the Harvard Dataverse as well as GitHub (`https://github.com/tamdur/ACRIM-Gap`). Satellite data for the ACRIM1/SMM, ACRIM2/UARS, ERBS/ERBE, and Nimbus-7/HF missions were accessed from the NOAA National Centers for Environmental Information at `https://www.ngdc.noaa.gov/stp/solar/solarirrad.html` (last accessed 20 March 2023). Data for the fused A+B corrected series version 8.0 of the VIRGO Experiment on the cooperative ESA/NASA Mission SoHO from VIRGO Team through PMOD/WRC, Davos, Switzerland, are retrieved from `ftp://ftp.pmodwrc.ch/pub/data/irradiance/virgo/TSI/` (last accessed 13 October 2022). Daily total sunspot numbers are retrieved from `https://www.sidc.be/silso/datafiles` (last accessed 20 March 2023). The University of Bremen composite Mg-II Index version 5 is retrieved from `https://www.iup.uni-bremen.de/UVSAT/Datasets/mgii` (last accessed 20 March 2023).

Acknowledgments

T. Amdur was supported by a NASA FINESST grant 80NSSC19K1327.

References

Bernanke, B. S., Boivin, J., & Eliasz, P. (2005). Measuring the effects of monetary policy: a factor-augmented vector autoregressive (FAVAR) approach. *The Quarterly journal of economics*, *120*(1), 387–422.

Blake, A. P., Mumtaz, H., et al. (2012). Applied Bayesian econometrics for central bankers. *Technical Books*.

Butler, J. J., Johnson, B. C., Rice, J. P., Shirley, E. L., & Barnes, R. (2008). Sources of differences in on-orbital total solar irradiance measurements and description of a proposed laboratory intercomparison. *Journal of research of the National Institute of Standards and Technology*, *113*(4), 187.

Carter, C. K., & Kohn, R. (1994). On Gibbs sampling for state space models. *Biometrika*, *81*(3), 541–553.

Coddington, O., Lean, J., Pilewskie, P., Snow, M., & Lindholm, D. (2016). A solar irradiance climate data record. *Bulletin of the American Meteorological Society*, *97*(7), 1265–1282.

Dewitte, S., Cornelis, J., & Meftah, M. (2022). Centennial total solar irradiance variation. *Remote Sensing*, *14*(5), 1072.

Dewitte, S., & Nevens, S. (2016). The total solar irradiance climate data record. *The Astrophysical Journal*, *830*(1), 25.

Dudok de Wit, T., Kopp, G., Fröhlich, C., & Schöll, M. (2017). Methodology to create a new total solar irradiance record: Making a composite out of multiple data records. *Geophysical Research Letters*, *44*(3), 1196–1203.

Finsterle, W., Montillet, J. P., Schmutz, W., Šikonja, R., Kolar, L., & Treven, L. (2021). The total solar irradiance during the recent solar minimum period measured by SOHO/VIRGO. *Scientific reports*, *11*(1), 1–10.

Fröhlich, C. (2006). Solar irradiance variability since 1978. In *Solar variability and planetary climates* (pp. 53–65). Springer.

Fröhlich, C. (2009). Evidence of a long-term trend in total solar irradiance. *Astronomy & Astrophysics*, *501*(3), L27–L30.

Fröhlich, C., & Lean, J. (2004). Solar radiative output and its variability: evidence and mechanisms. *The Astronomy and Astrophysics Review*, *12*(4), 273–320.

Gelman, A., Carlin, J. B., Stern, H. S., Dunson, D. B., Vehtari, A., & Rubin, D. B. (2013). *Bayesian data analysis*. CRC press.

Gueymard, C. A. (2018). A reevaluation of the solar constant based on a 42-year total solar irradiance time series and a reconciliation of spaceborne observations. *Solar Energy*, *168*, 2–9.

Hickey, J., Stowe, L., Jacobowitz, H., Pellegrino, P., Maschhoff, R., House, F., & Vonder Haar, T. (1980). Initial solar irradiance determinations from Nimbus 7 cavity radiometer measurements. *Science*, *208*(4441), 281–283.

Hoyt, D. V., Kyle, H. L., Hickey, J. R., & Maschhoff, R. H. (1992). The Nimbus 7 solar total irradiance: A new algorithm for its derivation. *Journal of Geophysical Research: Space Physics*, *97*(A1), 51–63.

Kopp, G. (2014). An assessment of the solar irradiance record for climate studies. *Journal of Space Weather and Space Climate*, *4*, A14.

Kopp, G. (2016). Magnitudes and timescales of total solar irradiance variability. *Journal of space weather and space climate*, *6*, A30.

Kopp, G., Krivova, N., Wu, C., & Lean, J. (2016). The impact of the revised sunspot record on solar irradiance reconstructions. *Solar Physics*, *291*, 2951–2965.

Kopp, G., & Lean, J. L. (2011). A new, lower value of total solar irradiance: Evidence and climate significance. *Geophysical Research Letters*, *38*(1).

Krivova, N., Solanki, S., & Wenzler, T. (2009). ACRIM-gap and total solar irradiance revisited: Is there a secular trend between 1986 and 1996? *Geophysical Research Letters*, *36*(20).

Lean, J. (2000). Evolution of the Sun's spectral irradiance since the Maunder Minimum. *Geophysical Research Letters*, *27*(16), 2425–2428.

Lean, J., Beer, J., & Bradley, R. (1995). Reconstruction of solar irradiance since 1610: Implications for climate change. *Geophysical Research Letters*, *22*(23), 3195–3198.

Lee, R. B., Barkstrom, B. R., & Cess, R. D. (1987, Aug). Characteristics of the earth radiation budget experiment solar monitors. *Appl. Opt.*, *26*(15), 3090–3096. Retrieved from `http://opg.optica.org/ao/abstract.cfm?URI=ao-26-15-3090` doi: 10.1364/AO.26.003090

Lee III, R. B., Gibson, M. A., Wilson, R. S., & Thomas, S. (1995). Long-term total solar irradiance variability during sunspot cycle 22. *Journal of Geophysical Research: Space Physics*, *100*(A2), 1667–1675.

Lockwood, M., & Ball, W. T. (2020). Placing limits on long-term variations in quiet-Sun irradiance and their contribution to total solar irradiance and solar radiative forcing of climate. *Proceedings of the Royal Society A*, *476*(2238), 20200077.

Lockwood, M., & Fröhlich, C. (2008). Recent oppositely directed trends in solar climate forcings and the global mean surface air temperature. II. Different reconstructions of the total solar irradiance variation and dependence on response time scale. *Proceedings of the Royal Society A: Mathematical, Physical and Engineering Sciences*, *464*(2094), 1367–1385.

Montillet, J.-P., Finsterle, W., Kermarrec, G., Sikonja, R., Haberreiter, M., Schmutz, W., & Dudok de Wit, T. (2022). Data fusion of total solar irradiance composite time series using 41 years of satellite measurements. *Journal of Geophysical Research: Atmospheres*, *127*(13), e2021JD036146. Retrieved from `https://agupubs.onlinelibrary.wiley.com/doi/abs/10.1029/2021JD036146` (e2021JD036146 2021JD036146) doi: https://doi.org/10.1029/2021JD036146

Pankratz, A. (2012). *Forecasting with dynamic regression models*. John Wiley &

Sons.

Pap, J. M., Willson, R. C., Fröhlich, C., Donnelly, R. F., & Puga, L. (1994). Long-term variations in total solar irradiance. *Solar Physics*, *152*(1), 13–21.

Scafetta, N., & Willson, R. C. (2009). ACRIM-gap and TSI trend issue resolved using a surface magnetic flux TSI proxy model. *Geophysical Research Letters*, *36*(5).

Scafetta, N., & Willson, R. C. (2014). ACRIM total solar irradiance satellite composite validation versus TSI proxy models. *Astrophysics and Space Science*, *350*(2), 421–442.

Scafetta, N., & Willson, R. C. (2019). Comparison of decadal trends among total solar irradiance composites of satellite observations. *Advances in Astronomy*, *2019*.

Scafetta, N., Willson, R. C., Lee, J. N., & Wu, D. L. (2019). Modeling quiet solar luminosity variability from TSI satellite measurements and proxy models during 1980–2018. *Remote Sensing*, *11*(21), 2569.

Shapiro, A., Solanki, S. K., Krivova, N. A., Cameron, R. H., Yeo, K. L., & Schmutz, W. (2017). The nature of solar brightness variations. *Nature Astronomy*, *1*(9), 612–616.

SILSO World Data Center. (1984-1996). The international sunspot number. *International Sunspot Number Monthly Bulletin and online catalogue*.

Thuillier, G., DeLand, M., Shapiro, A., Schmutz, W., Bolsee, D., & Melo, S. (2012). The solar spectral irradiance as a function of the Mg II index for atmosphere and climate modelling. *Solar Physics*, *277*(2), 245–266.

Tingley, M. P., Craigmile, P. F., Haran, M., Li, B., Mannshardt, E., & Rajaratnam, B. (2012). Piecing together the past: statistical insights into paleoclimatic reconstructions. *Quaternary Science Reviews*, *35*, 1–22.

Tingley, M. P., & Huybers, P. (2010). A Bayesian algorithm for reconstructing climate anomalies in space and time. Part II: Comparison with the regularized expectation–maximization algorithm. *Journal of Climate*, *23*(10), 2782–2800.

Viereck, R., Puga, L., McMullin, D., Judge, D., Weber, M., & Tobiska, W. K. (2001). The Mg II index: A proxy for solar EUV. *Geophysical Research Letters*, *28*(7), 1343–1346.

Willson, R. C. (1997). Total solar irradiance trend during solar cycles 21 and 22. *Science*, *277*(5334), 1963–1965.

Willson, R. C. (2014). ACRIM3 and the total solar irradiance database. *Astrophysics and Space Science*, *352*(2), 341–352.

Willson, R. C., & Hudson, H. S. (1991). The Sun's luminosity over a complete solar cycle. *Nature*, *351*(6321), 42–44.

Willson, R. C., & Mordvinov, A. V. (2003). Secular total solar irradiance trend during solar cycles 21–23. *Geophysical Research Letters*, *30*(5).

Woods, T. N., Eparvier, F. G., Harder, J., & Snow, M. (2018). Decoupling solar variability and instrument trends using the Multiple Same-Irradiance-Level (MuSIL) analysis technique. *Solar physics*, *293*(5), 1–21.

Yeo, K., Krivova, N., & Solanki, S. (2017). EMPIRE: A robust empirical reconstruction of solar irradiance variability. *Journal of Geophysical Research: Space Physics*, *122*(4), 3888–3914.

Yeo, K., Krivova, N., Solanki, S., & Glassmeier, K. (2014). Reconstruction of total and spectral solar irradiance from 1974 to 2013 based on KPVT, SoHO/MDI, and SDO/HMI observations. *Astronomy & Astrophysics*, *570*, A85.